Oscillations of a liquid bridge resulting from the coalescence of two droplets

Véronique Chireux, David Fabre, Frédéric Risso, Philippe Tordjeman

http://dx.doi.org/10.1063/1.4922474

Oscillations of a liquid bridge resulting from the coalescence of two droplets

Véronique Chireux, David Fabre, Frédéric Risso, and Philippe Tordjeman
Institut de Mécanique des Fluides de Toulouse, Université de Toulouse and CNRS, Toulouse, France

The inertial oscillations of a bridge of liquid maintained between two disks are studied under condition of negligible gravity. Both experimental and theoretical results are reported. In the experiment, the bridge is formed by the coalescence of two droplets so that its static equilibrium shape is either concave or convex depending on its length. After coalescence, the bridge performs weakly damped oscillations until it reaches its equilibrium shape. Four modes of oscillations are extracted from digital processing of images recorded by means of a high-speed camera. Their frequency and damping rate are determined and found to be independent of the initial conditions that fix the amplitudes of each mode. Concurrently, the eigen modes of oscillations of a non-cylindrical bridge have been computed by assuming inviscid flow and small amplitude oscillations. The agreement between theoretical and measured frequencies confirms that the experimental modes correspond to the eigenmodes of the linear inviscid theory. Their characteristics turn out to be significantly different from that of a cylindrical bridge. In particular, the eigenfrequencies scale as $\sqrt{\gamma/\rho R_m^3}$, where γ is the surface tension, ρ the liquid density, and R_m the radius at the middle of the bridge, which characterizes the shrunk/swollen character of the mean shape.

I. INTRODUCTION

Surface-tension driven flows play a major role in droplet formation.[1] When viscous effects are low, the dynamics of the interface is characterized by the inertial modes of oscillations, which can be used to describe its behavior in many different situations. By considering the dynamics of a column of fluid, such an approach has been developed to address the primary formation of droplets from jets, since the pioneering work of Rayleigh,[2,3] and is also involved in the fragmentation of liquid filaments.[4] Secondary breakup is also concerned since the fragmentation of droplets or bubbles in a turbulent flow has been shown to result from excitation of inertial modes by turbulent eddies.[5,6] Concerning droplets, the eigenmodes of oscillations have been determined theoretically for free[7,8] or attached droplets[9–13] in the absence of gravity and investigated numerically for rising droplets.[14] Experiments that match theoretical predictions are difficult to realize because of practical difficulties to levitate[15] or attach a droplet[16] and of possible contamination by surfactant.[17] Concerning liquid columns, the eigenmodes of an infinite liquid filament have been known for a long time[18] while those of a bridge of finite length have been determined theoretically[19] and investigated experimentally[20] only recently for oscillations around a cylindrical mean shape. The stability of non-cylindrical liquid bridges has been considered in several works[21,22] but the eigenmodes of oscillations have not been determined so far.

Despite its high fundamental interest and the number of applications concerned, both in classic domains (painting, irrigation, and fuel injection) as well as in new technology (ink printing[23] and float zone method for crystal growth[24]), many aspects of the dynamics of liquid bridges are still unknown. The objective of the present work is to determine the eigenmodes of vibration of non-cylindrical liquid bridges in situations where gravity and viscosity play a minor role. Both experimental and theoretical results are reported. In the experiment, the liquid bridge is produced

by the coalescence of two liquid drops mounted on capillary tubes. After formation, the bridge experiences non-axisymmetrical oscillations around its equilibrium shape. The length of the bridge, which is fixed by the initial drop sizes, determines the equilibrium shape: concave for short bridge and convex for large ones. Note that the convexity retards the onset of the static instability and allows to study stable bridges of longer length. The oscillations essentially involved four modes, which are distinguished from each other, thanks to a method taking advantage of their symmetry differences. Concurrently, the theoretical eigenmodes corresponding to the same equilibrium shapes are computed numerically under the assumption of potential flow and small oscillation amplitudes. A good agreement is obtained between the theory and the experiment results, which turn out to be very robust regarding the initial conditions. Thus, the assumptions made to derive the theory are validated and the relevance of the present numerical method is established. Moreover, the experimental method is proved to be well suited to reveal the fundamental dynamic characteristic of bridge oscillations.

The paper is organized as follows. The configuration under investigation is described in Sec. II as well as the experimental setup and measurement methods. Experimental results concerning frequencies and damping rates are presented in Sec. III. The theoretical approach, the numerical method, and predicted eigenfrequencies are presented in Sec. IV and detailed in the Appendices. Experimental and theoretical results are compared and discussed in Sec. V.

II. EXPERIMENTAL CONFIGURATION AND MEASUREMENT METHODS

In practice, it is difficult to generate a liquid bridge in order to study the free oscillations that result from an initial shape perturbation. The following original experimental technique has been developed. Two droplets are formed at the extremities of two facing horizontal capillary tubes (Figure 1) by injecting liquid by means of a syringe pump. The pump is stopped just before the two drops touch each other. The drops, however, continue growing because of the residual excess of pressure in the deformable tubes that supply liquid from the syringe to the capillaries. Note that this growth is very slow ($<100\ \mu l\ h^{-1}$) so that the subsequent increase in the droplet volume during the total duration of an experimental run (<100 ms) is negligible. The droplets then come into contact and coalesce.

Figure 2 shows a typical sequence of images of the process that occurs after the coalescence. We first observe a transient stage ((a)-(c)), during which the neck connecting the two drops enlarges. This first stage lasts until the shape disturbance generated at the initial contact point of the two droplets reaches the capillary tubes. Then, we are left with a liquid bridge joining two capillaries which experiences weakly damped shape oscillations ((d)-(i)). The amplitudes of the modes of oscillations that are excited depend on the initial geometry of the drops and on the details of both

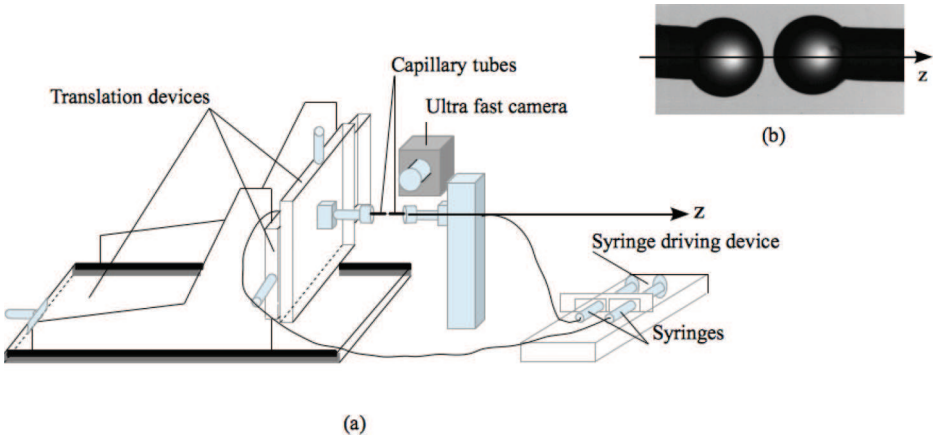

FIG. 1. (a) Schematic of the experimental arrangement. (b) Photograph of the two initial drops attached to the capillary extremities before coalescence.

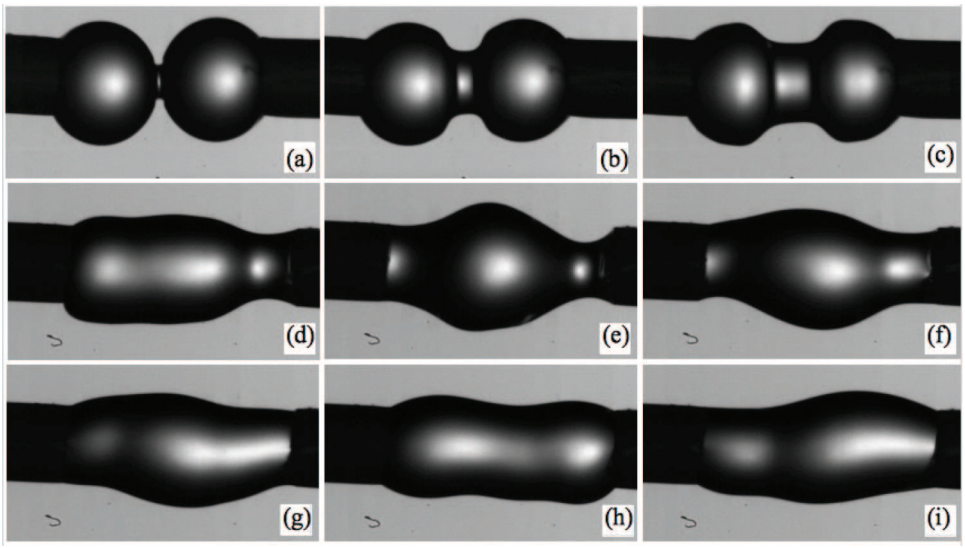

FIG. 2. Evolution of the liquid bridge after coalescence of the two drops. ((a)-(c)) Growth of the neck that connects the two drops. ((d)-(i)) Oscillations of the liquid bridge. (a) $t = 0$; (b) $t = 0.16$ ms; (c) $t = 0.32$ ms; (d) $t = 0.56$ ms; (e) $t = 1.08$ ms; (f) $t = 1.64$ ms; (g) $t = 1.84$ ms; (h) $t = 2.24$ ms; and (i) $t = 3.24$ ms.

the coalescence process and the transient stage. In particular, the amplitudes of the modes that are antisymmetric relative to the mid-plane $z = L/2$ depend on the size difference between the two drops. Also, the amplitudes of the modes that are not symmetric relative to the z-axis depend on the minute misalignment of the two capillary tubes. Eventually, when the excess of surface energy has been dissipated, the bridge reaches a static equilibrium that reveals the mean shape around which the oscillations have taken place (Figure 3).

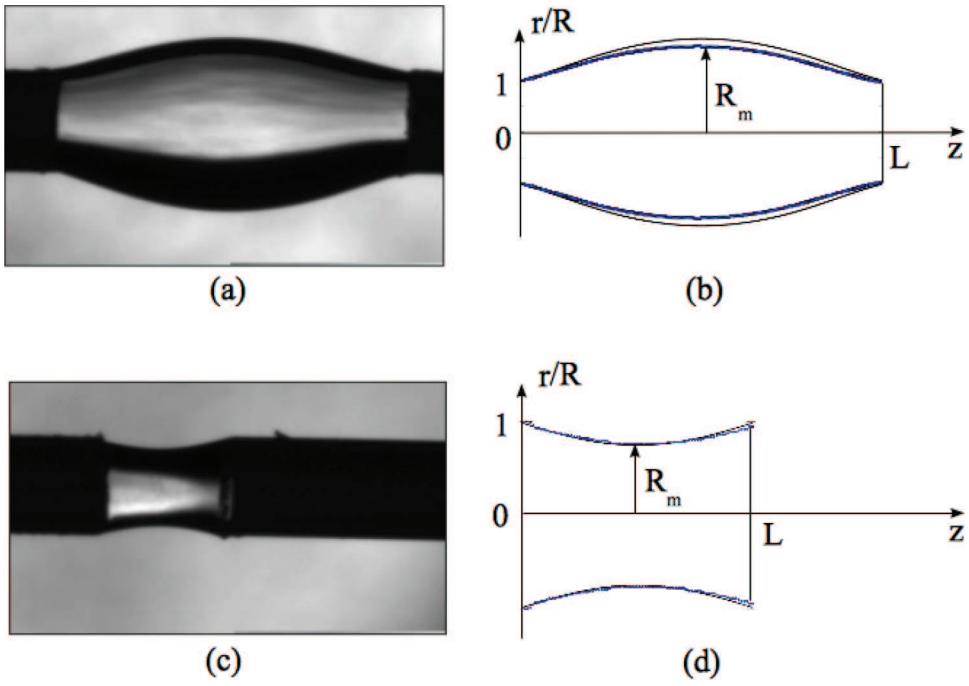

FIG. 3. Static shapes of the bridge at equilibrium. ((a) and (b)) Convex shape for $L^* = 6.6 > L_c^*$. ((c) and (d)) Concave shape for $L^* < 2.3$. ((a) and (c)) Digital images. ((b) and (d)) Experimental detected contours (points) compared to theory (plain line).

The capillary tubes are made of PEEK (PolyEtherEtherKetone). Their axes are aligned along the horizontal z-direction, thanks to a three-axis translating system. Experiments have been conducted with capillary tubes of two different outer diameters, $R = 180 \pm 5$ μm or $R = 305 \pm 5$ μm, but with the same inner diameter, $R_{in} = 25$ μm. It has been checked that the gas-liquid interface remains attached to the outer edge of the capillaries and that the angle it makes with the tube is free to change. Furthermore, because R_{in}^2 is less than 2% of R^2, it can be assumed a non-slip velocity boundary condition for the liquid on the capillaries.

The experiments are conducted at room temperature (20 ± 1 °C). In most of the tests, the liquid was distilled water: dynamic viscosity $\mu = 1.0 \times 10^{-6}$ Pa s, density $\rho = 1.0$ kg m^{-3}, and surface tension $\gamma = 70$ N m^{-1}. For the case $R = 180$ μm, additional tests have been carried out with aqueous solutions of $MgSO_4$ of various concentrations: 0.4 gl^{-1}, 0.8 gl^{-1}, or 4 gl^{-1}. At such concentrations, viscosity, density, and surface tension are not significantly different from those of pure water. $MgSO_4$ is thus expected to have no influence on the proper dynamic of the bridge in the linear regime. However, the presence of $MgSO_4$ is known to delay the coalescence of air bubbles in water.[25] Since it affects the coalescence process, it is therefore expected to change the amplitudes of excited eigenmodes. Comparing tests done with pure water or $MgSO_4$ solutions is a way to assess whether the results are affected or not by the initial conditions.

The liquid is lighted by means of a Light-Emitting Diode (LED) backlight (not represented in the schematic of Figure 1). Shadow images of the drops or the bridge are recorded, thanks to a high-speed camera (V1210 Phantom). The framing rate and the exposure time are close to 50 000 frames per second and 16 μs, respectively. The image size is 512×320 pixels, which approximately corresponds to a visualization window of 2.5 mm in the axial direction and 1.6 mm in the radial one. This leads to a time resolution of 20 μs and a spatial resolution of 5 μm. On each image, the contour of the gas-liquid interface in the vertical plane of view is detected by classic digital image processing.

The present experiments therefore allow the study of a liquid bridge of volume V attached to the edges of two facing solid disks of radius R separated by a distance L (Figure 4). The fluid is a Newtonian liquid with density ρ and kinematic viscosity μ. The bridge is surrounded by a gas of negligible density and viscosity. The surface tension γ is assumed to be constant. If we also consider the acceleration of gravity g, the static shape of the bridge and its oscillations around its equilibrium shape depend on four dimensionless numbers:

- the Bond number, $B_o = \rho g R^2 \gamma^{-1}$, compares gravity to surface tension forces;
- the Ohnesorge number, $\mu/\sqrt{(\rho R \gamma)}$, compares inertia to viscous stresses in the flow driven by surface tension;
- the slenderness ratio, $L^* = L/R$, compares the length of the bridge to its radius;
- the reduced volume, $V^* = V/(\pi R^2 L)$, compares the volume of the actual bridge to that of a circular cylinder of same radius R and length L.

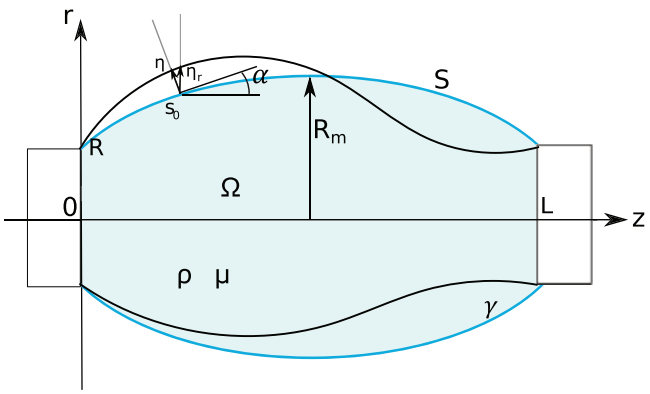

FIG. 4. (a) Schematic of the problem under investigation and notation.

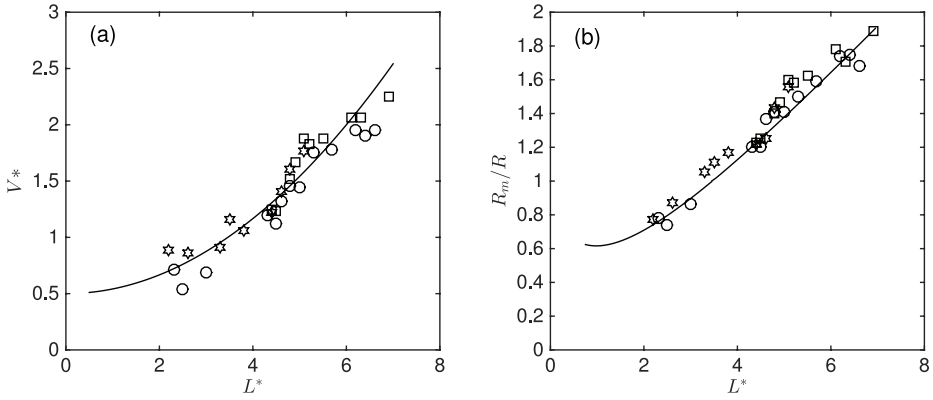

FIG. 5. Geometrical characteristics of the equilibrium shape of the bridge. (a) Reduced volume V^*: symbols correspond to measurements and line to Eq. (1). (b) Radius in the middle of the bridge R_m/R versus L^*: symbols correspond to measurements and line to theoretical result obtained in Sec. IV A. Circles correspond to initial drops of same size for $R = 180$ μm, squares to initial drops having different sizes for $R = 180$ μm, and stars to initial drops having different sizes for $R = 305$ μm.

Both the Bond number and the Ohnesorge number are less then 10^{-2}, which means that gravity can be neglected and that viscosity is expected to only affect the long term evolution by slowly damping the oscillations.

Since bridge is formed by the coalescence of two drops, the slenderness ratio and the reduced volume cannot be chosen independently. Considering that the volume of the bridge is the total volume of the two initial drops, we find the following relation between L^* and V^* (see detail in Appendix A):

$$V^* = \frac{1}{2}(1 + \frac{L^{*2}}{12}). \tag{1}$$

Figure 5(a) shows the actual values of V^* obtained from the measurement of the bridge volume as a function of L^*. The agreement with theoretical expression (1) is very good regardless of whether the two drops have the same size or not.

The distance between the capillaries has been varied so that the slenderness ratio L^* covered the range from 2 to 7 (by increments of 0.1 for small values of L and increments of 0.2 for large ones). The size of the two initial drops ($200 \leq R_g \leq 400$ μm) is not always the same, and the ratio of their radii is varied between 1 and 1.6 in order to vary the departure from symmetry of the initial conditions. Experiments are repeated once for each value to L^*. The whole set of experiments represents 50 sequences of 2000–12 000 images each.

From Eq. (1), $V^* = 1$ for $L^* = L_c^* = \sqrt{12} \approx 3.46$. The equilibrium shape of the bridge is found to be concave for $L^* \leq L_c^*$, cylindrical for $L^* = L_c^*$, and convex for $L^* \geq L_c^*$ (Figure 3). A relevant length scale to characterize the static shape is the radius R_m at the middle of the bridge, which is smaller than R for $L^* \leq L_c^*$ and larger for $L^* \geq L_c^*$. Figure 5(b) shows the evolution of R_m/R as a function of L^*. In the range investigated, R_m is found to be almost proportional to L. It is worth noting that the final shape of the bridge turns out to depend only on L^*. It is not influenced either by the various ratios of initial drop sizes investigated or by the presence of $MgSO_4$ dissolved in water. It is neither influenced by the radius R of the capillary that is used. Finally, no significant difference is observed between the upper and lower detected contours of the bridge, which confirms that effect of gravity can be neglected.

For a given point M of the interface defined by its cylindrical coordinates (r, θ, z), the amplitude of the deformation is defined by the radial displacement η_r of the interface relative to its equilibrium location r_0: $\eta_r(z,\theta,t) = r(z,\theta,t) - r_0(z,\theta,t)$. Figure 6 shows typical time series of η_r for four different points in the plane of view of the camera ($\theta = 0$ or π). The signals are quite complex and clearly involve several different frequencies. This is not surprising since the initial conditions resulting from the coalescence of two droplets are not expected to select a single mode of oscillation.

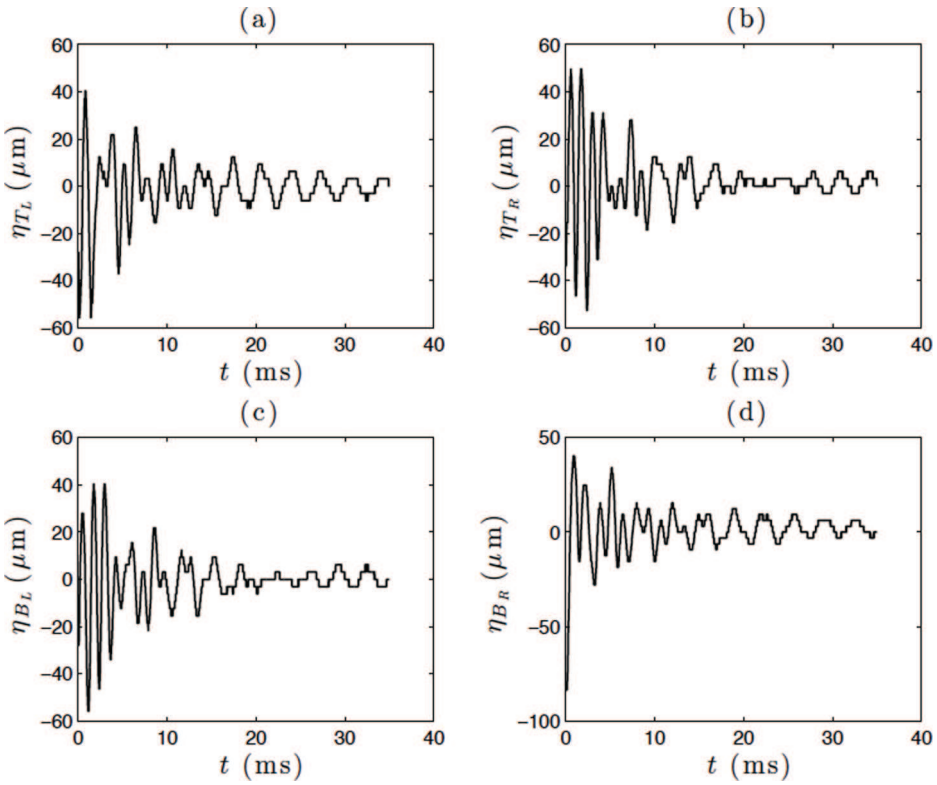

FIG. 6. Typical experimental time series of the interface radial displacement η_r for case $L^* = 4.6$ at points T_L, T_R, B_L, and B_R, which are defined in Figure 7.

For given couple (L^*, V^*), the linear theory of oscillations (see Sec. IV) shows that there exists a denumerable family of modes defined by two integers (m,n), where m defines the number of nodes in the azimuthal direction and n the number of nodes in the longitudinal direction. Modes with $m = 0$ are symmetric by rotation around z-axis, whereas modes with $m \neq 0$ are not. Modes with even n are symmetric relative to the mid-plane $z = L/2$ while modes with odd n are antisymmetric relative to this plane. Since modes of low m and n involve smaller interface curvatures and velocity gradients, they require less energy to be excited and are less damped by viscous dissipation. We will therefore assume that only the four lowest modes corresponding to each possible symmetry, $(m,n) = (1,0)$, $(0,1)$, $(1,1)$, and $(0,2)$, are involved in the bridge oscillations that take place after the initial transient stage. The deformation amplitude of the interface can hence be decomposed into the contributions of these four modes,

$$\eta_r(z,\theta,t) = \eta_{0s}(z,t) + \eta_{0a}(z,t) + \eta_{1s}(z,t)\cos(\theta) + \eta_{1a}(z,t)\cos(\theta) + \eta^*_{1s}(z,t)\sin(\theta) + \eta^*_{1a}(z,t)\sin(\theta), \tag{2}$$

where the first subscript of the η's denotes the azimuthal number m, and the second one is s for symmetric modes (even n) and a for antisymmetric modes (odd n) relative to the plane $z = L/2$. The correspondence between the two notations is given in Figure 7. The terms η_{1s} and η_{1a} correspond to oscillations in the vertical plane, while η^*_{1s} and η^*_{1a} correspond to oscillations in the horizontal plane. The latter are not measured because we only see the projection of the interface in the plane $\theta = 0$ or π.

Taking advantage of the symmetries described above, it is possible to decompose the surface deformation into the contribution of the four modes 0s, 0a, 1s, and 1a. Let us consider four particular points T_L, T_R, B_L, and B_R of respective coordinates $(z,\theta) = (+z_0,0), (L - z_0,0), (+z_0,\pi)$, and $(L - z_0,\pi)$, which are illustrated in Figure 7. The following linear combinations of the displacements of these four points achieve the decomposition:

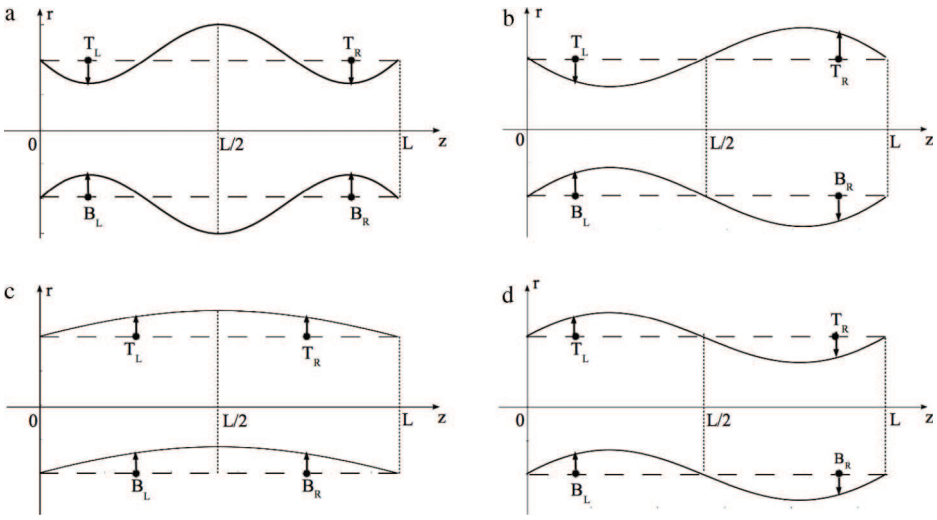

FIG. 7. Illustration of the geometry of the four leading modes and locations of the particular points (T_L, T_R, B_L, and B_R) used for the experimental mode extraction procedure. The continuous curves show the shape of the four modes 0s, 0a, 1s, and 1a analytically derived from the inviscid linear theory for a cylindrical bridge (see Sec. IV B and Appendix C for details about the theory). (a) Mode $0s$ (m = 0, n = 2). (b) Mode $0a$ (m = 0, n = 1). (c) Mode $1s$ (m = 1, n = 0). (d) Mode $1a$ (m = 1, n = 1).

$$\eta_{0s}(z_0,t) = \frac{\eta(T_R) + \eta(T_L) + \eta(B_R) + \eta(B_L)}{4}, \tag{3}$$

$$\eta_{0a}(z_0,t) = \frac{\eta(T_R) - \eta(T_L) + \eta(B_R) - \eta(B_L)}{4}, \tag{4}$$

$$\eta_{1s}(z_0,t) = \frac{\eta(T_R) + \eta(T_L) - \eta(B_R) - \eta(B_L)}{4\,\cos(\theta_{1s})}, \tag{5}$$

$$\eta_{1a}(z_0,t) = \frac{\eta(T_R) - \eta(T_L) + \eta(B_R) - \eta(B_L)}{4\,\cos(\theta_{1s})}. \tag{6}$$

This decomposition involves the parameter z_0 that defines the axial locations of the considered measurement points. Ideally, it should be chosen at the antinode of each mode in order to get the largest amplitude and thereby improve the accuracy. Practically, z_0 has been empirically adjusted in all test runs in order to enhance the amplitude of the measured signals. We are thus not able to locate each mode relatively to z_0. Moreover, since a single plane of view is available, the value of θ_{1s} is not known. Consequently, the four amplitudes η_{0s}, η_{0a}, η_{1s}, and η_{1a} obtained by the present method are determined except for an unknown constant factor. It will be, therefore, not possible to compare the relative amplitudes of the various modes nor to investigate nonlinear effects arising at large amplitude. However, as long as we consider small amplitudes that belong to the linear regime of oscillations, we should be able to determine the frequency and the damping rate of the various modes.

Figure 8 shows the time evolution of the mode amplitudes determined from the four signals represented in Figure 6. In contrast with raw signals, each signal now clearly exhibits a single dominant frequency. We can, therefore, conclude that the present technique allows to isolate the four lowest eigenmodes of oscillation. When the amplitude is large enough, as it is the case for η_{0s} and η_{1a} in the example shown in Figure 8, the oscillations are, as expected, observed to be regularly damped. The signals are thus well described by the following equation:

$$\eta_{ij}(t) = c + ae^{-\beta_{ij}t}cos(\omega_{ij}t + \phi_{ij}). \tag{7}$$

Figure 9(a) shows the fitting of η_{0s} by Eq. (7), while Figure 9(b) presents the spectrum of η_{0s} computed by means of digital Fourier transform. The frequency ω of the corresponding eigenmode can be obtained from either the value found from the best fitting by Eq. (7) or at the peak value Sp_{max} of the spectrum Sp. The values obtained by the two different methods are in agreement within

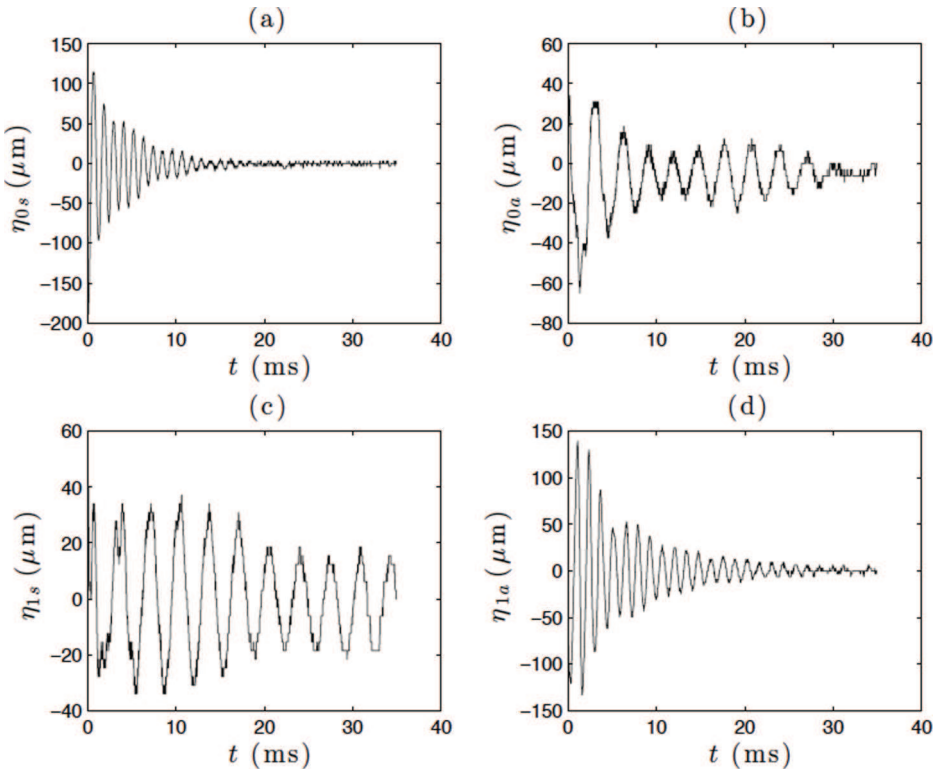

FIG. 8. Time evolutions of the amplitudes of modes 0s, 0a, 1s, and 1a after application of the extraction method from the experimental signals at points T_L, T_R, B_L, and B_R presented in Figure 6.

1%. Similarly, the damping rate β can be obtained either from the fitting or from the width of the peak of the spectrum between $Sp_{max}(1 - 1/\sqrt{2})$ and $Sp_{max}(1 + 1/\sqrt{2})$. The two values agree within 10%.

When the amplitudes are lower, a secondary frequency may hide the damping, as it can be seen in Figures 8(b) and 8(c). This is observed for modes η_{0a} and η_{1s}, which have close eigen frequencies. In the considered example, the main frequency and secondary frequency of η_{0a} are found to be 2.1×10^3 rad/s and 1.8×10^3 rad/s while those of η_{1s} are 1.8×10^3 rad/s and 2.1×10^3 rad/s. The secondary frequency of a signal therefore corresponds to the main frequency of the other, and vice versa. This can either be the signature of weak non-linear interactions between two eigenmodes that

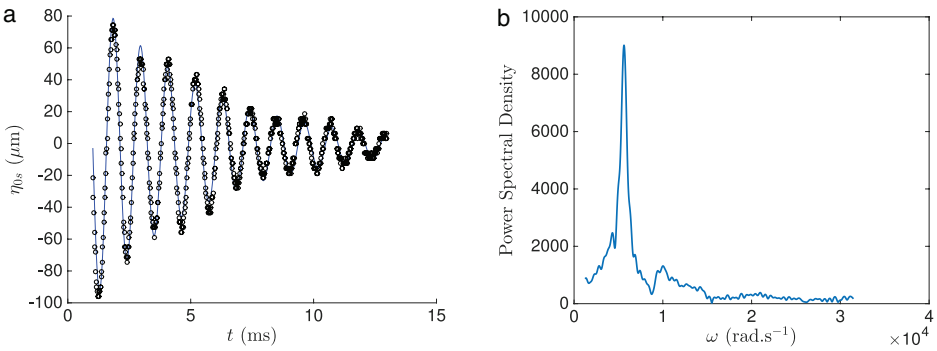

FIG. 9. Illustration of the two methods for experimental determination of frequency and damping rate. The present example corresponds to mode 0s for $L^* = 4.6$. (a) Fitting of time evolution of mode amplitude by Eq. (7) with $\omega = 5.6 \times 10^3$ rad s^{-1} and $\beta = 220$ s^{-1}. (b) Spectrum of the signal: the abscissa of the main peak is $\omega = 5.65 \times 10^3$ rad s^{-1} and then its width leads to $\beta = 240$ s^{-1}.

have close frequencies or result from the difficulty to experimentally disentangle them. Comparisons that will be done later with the linear theory will show that the measured frequencies are not affected by the possible existence of weak non-linear interactions.

In the following, the experimental values of the eigenfrequencies and damping rates of the four modes 0s, 1s, 0a, and 1a have been obtained by means of the procedure that has been described in this section, using either the fitting of the time signals or their spectrum. Frequencies are determined within ±2%. The accuracy of damping rates strongly depends on each particular signal and will be shown by error bars on the corresponding plots.

III. EXPERIMENTAL RESULTS FOR THE FREQUENCY AND THE DAMPING RATE

Figure 10 shows the measured angular frequencies ω_{ij} and damping rates β_{ij} of the four modes for all experimental conditions as functions of the slenderness ratio L^*. The frequencies are normalized by $\omega_R = \sqrt{\gamma/\rho R^3}$ and the damping rate by $\beta_R = \eta/\rho R^2$ in order to allow the comparison between the two considered values of the radius R. First, it is remarkable that the measured frequencies and damping rates of each mode gather on a single curve whatever the value of R, the presence or the absence of $MgSO_4$ or the size differences between the two initial droplets. The experimental results are therefore robust with regard to the initial conditions. Measured frequencies and damping rates thus turn out to not depend on the amplitudes of the excited modes and can be considered as characteristic of the eigenmodes of oscillation of the liquid bridge.

Considering the frequencies, we observe that the four modes can be grouped two by two. On the one hand, the frequencies of modes 0s and 1a are larger and converge towards each other at large L^*. On the other hand, the frequencies of modes 0a and 1s are lower and converge towards each other at large L^*. The measurements of the damping rate are less accurate since their values are in any case at least 10 times smaller than the frequencies, confirming that the oscillations are weakly damped. Despite the scattering of the measurement, a grouping of the values similar to that of the frequencies seems also to be observed for the damping rates, especially for modes 0s and 1a.

Both the normalized frequency ω_{ij}/ω_R and the damping rate β_{ij}/β_R of each mode strongly depend on the slenderness ratio L^*. For such a bridge of finite length, the mode properties do not only depend upon the length scale R. They also depend upon the bridge length L and the bridge longitudinal curvature, which can be characterized by R_m. In Sec. IV, we shall derive the eigenmodes of bridge oscillations from the inviscid linear theory, since the case of a finite bridge of non-cylindrical mean shape has never been treated in previous works. Comparisons between theory and measurements will allow to assess the assumptions made in the interpretation of the experiments: boundary conditions at the bridge extremities for both the fluid motion and the interface,

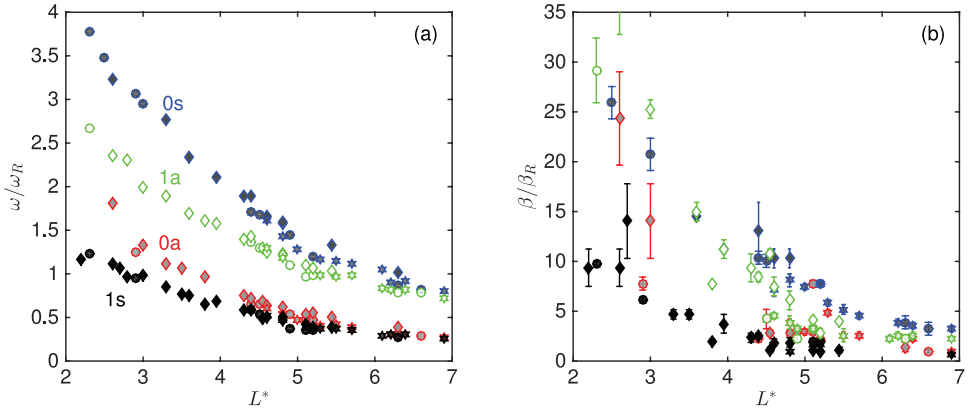

FIG. 10. Normalized experimental frequencies ω_{ij}/ω_R (a) and damping rates β_{ij}/β_R (b) of modes 0s, 0a, 1s, and 1a as a function of the slenderness ratio L^*. Circles: water with $R = 180$ μm. Stars: MgSO4 solution with $R = 180$ μm. Diamonds: water with $R = 350$ μm. Dark grey (blue) symbols: mode 0s. Light grey (red) symbols: mode 0a. Black symbols: mode 1s. Empty (green) symbols: mode 1a.

negligible effects of gravity or of slight misalignments of the capillaries, and negligible non-linear effects related to finite oscillation amplitudes and of viscous dissipation upon the mode frequencies. Moreover, the theory may help us to understand the role of the particular curvature of the static shape of the bridge that results from its generation by coalescence of two droplets.

IV. THEORETICAL DERIVATION

A. Static shape of the bridge at equilibrium

The equilibrium shape of the surface $\mathcal{S}$ of a liquid bridge formed by the coalescence of two droplets is described in cylindrical coordinates by using one of the two following parametric representations: $r = r_0(z)$, or $[r,z] = [r(s_0), z(s_0)]$, where s_0 is the curvilinear coordinate along the surface (see Figure 4). The first parametrization is best suited to the description of the experimental results, while the second is best fitted to the theoretical description.

The surface $\mathcal{S}$ is governed by the Young-Laplace equation,

$$F = K - \frac{\Delta P}{\gamma} = 0 \text{ for } (z,r) \in \mathcal{S}, \tag{8}$$

which imposes that the curvature K of the surface takes a constant value prescribed by the pressure difference ΔP between the liquid within the bridge and the atmosphere. The equilibrium is realized for $K \equiv K_0$, where K_0 is given, using curvilinear coordinates, by

$$K_0 = -\frac{d\alpha}{ds_0} + \frac{\cos\alpha}{r}, \tag{9}$$

where α is the angle of the surface with respect to the z-axis (see Appendix B). The boundary conditions corresponding to attachment at the edges of the bounding disks are

$$r_0(z) = R \text{ for } z = 0 \text{ and } z = L. \tag{10}$$

Moreover, the nondimensional bridge volume V^* has to coincide with the one of two touching spherical drops as given by Eq. (1),

$$\frac{1}{R^2 L}\int_0^L r_0(z)^2 dz = \frac{1}{2}\left(1 + \frac{L^{*2}}{12}\right). \tag{11}$$

For a given slenderness ratio L^*, there exists a continuous family of axisymmetric shapes of constant curvature satisfying Laplace equation (8), parametrized by either the pressure difference ΔP or the volume V. Analytical expressions for these particular surfaces, called *onduloids*, are available in terms of elliptic integrals. Since our objective is also to compute the oscillations, it is more relevant for us to solve numerically the system formed by Eqs. (8)–(11). Several methods can be used. The most common is to use a shooting method: making a guess for ΔP and for the angle α_0 of the surface at the edge $[r,z] = [R,0]$, integrating numerically Eq. (8) in the axial direction, and iterating over ΔP and α_0 until the edge of the second plate at $(z,r) = (L,R)$ is reached for the prescribed value of the volume.

Here, we use a different and original method, based on an iterative deformation of the whole surface to reach the equilibrium shape. The method consists of the following steps:

1. Choose a guess value of Δ_P/γ and a guess contour $[z,r](s_0)$ passing through the two end points at $(z,r) = (0,R)$ and $(z,r) = (L,R)$ (for instance, a cylindrical shape). Compute the mean curvature K_0 of this guess contour from (8).
2. Expand the target function F as $F = F_0 + F_1 = 0$ with $F_0 = K_0 + \Delta_P/\gamma$ and deduce the correction $F_1 = K_1$ to the mean curvature needed to approach the actual equilibrium.
3. Thanks to formula (B5) expressing K_1 in terms of $\eta(s_0)$ and its derivatives, solve an inverse problem yielding the normal displacement $\eta(s_0)$ needed to cancel the curvature mismatch.
4. Deform the guess contour according to the computed value of η. Then, repeat iteratively steps 2–4 until $|F| < \epsilon$, where ϵ is a convergence threshold (say, $\epsilon = 10^{-12}$).

5. Compute the volume corresponding to the converged contour and compare with the desired value of the volume given by (11). In case of mismatch, change the value of Δ_P/γ and iterate the whole process until $V - V_0 < \epsilon$.

As the successive approximations of the curvature in step 2 are based on a Taylor expansion, the method is by essence a Newton-Raphson method, and the convergence is very fast (typically less than 8 iterations of steps 2–4). The method was originally implemented with Matlab and was subsequently introduced in the finite-element software FreeFem++ used to perform the eigenvalue computations (see Sec. IV B), in order to directly generate a mesh fitted to the bridge geometry. This method is quite versatile and can be used for a large class of problems of static equilibria, including gravity as pending drops, attached bubbles, menisci. . . .

Computed equilibrium shapes have been superimposed to experimental contours in Figure 3. Theoretical shapes compare well with measurements for both concave and convex bridges. Systematic comparisons have been carried out for all experimental runs. The computed values of the radius at the middle of the bridge, R_m, have been reported in Figure 5. They are in good agreement with experimental results.

B. Eigenmode analysis: Theory and numerical method

The purpose of this section is to determine the eigenmodes and eigenfrequencies of the inertial oscillations of a liquid bridge under the assumptions of potential flow and small amplitude oscillations. The solution for an infinite cylinder has been known for a long time.[18] The present case of a cylinder of finite length and non-cylindrical mean shape requires a numerical resolution, which has been achieved using a finite-element method implemented in the FreeFem++ software.[26–29]

For the description of the experimental results, the displacement of the bridge surface was defined as the displacement η_r in the radial direction. For the numerical approach, it is more convenient to introduce the displacement $\eta(s_0,\theta,t)$ relative to the mean surface $\mathcal{S}$ in the direction of the normal to the surface (Figure 4). The two quantities are related through $\eta = \eta_r \cos\alpha$.

The flow inside the bulk is assumed irrotational and described through a velocity potential $\phi(r,z,\theta,t)$. The velocity is directly deduced from the potential,

$$\mathbf{u} = \nabla\phi(z,r,\theta,t), \tag{12}$$

and the pressure is given by the linearized unsteady Bernoulli equation,

$$p = -\rho\frac{\partial\phi(z,r,\theta,t)}{\partial t}. \tag{13}$$

The unknown functions $[\phi(z,r,\theta,t);\eta(s_0,\theta,t)]$ are then governed by the following set of equations in the bulk domain Ω and boundary conditions and along the free surface $\mathcal{S}$ and on the disks at both bridge extremities:

$$\Delta\phi = 0 \text{ for } (z,r) \in \Omega, \tag{14}$$

$$\partial_z\phi = 0 \text{ for } z = 0 \text{ and } z = L, \tag{15}$$

$$\eta = 0 \text{ for } z = 0 \text{ and } z = L, \tag{16}$$

$$\mathbf{n}_0 \cdot \nabla\phi = \frac{\partial\eta}{\partial t} \text{ on } \mathcal{S}, \tag{17}$$

$$\gamma K_1 = -\rho\frac{\partial\phi}{\partial t} \quad \text{on } \mathcal{S}, \tag{18}$$

where $\mathbf{n}_0$ is the outward normal to the mean surface. Boundary conditions (15) and (16) mean no mass flux through the two disks that end the bridge, and fixed contact lines at the edge of the disks. Conditions (17) and (18) give the kinematical and dynamical boundary conditions on the free surface. The correction K_1 to the curvature of the surface relative to the mean shape can be written as (see Appendix B)

$$K_1(\eta) = -\frac{1}{r}\frac{\partial}{\partial s_0}\left(r\frac{\partial \eta}{\partial s_0}\right) - \left[\left(\frac{\partial \alpha}{\partial s_0}\right)^2 + \frac{\cos^2\alpha}{r^2} - \frac{m^2}{r^2}\right]\eta. \tag{19}$$

Owing to the linearity of the equations, the general solution can be searched as a sum of eigenmodes that can be written in a symbolic form as

$$[\phi(z,r,\theta,t);\eta(s_0,\theta,t)] = \sum_{m,n} A_{mn}\,[-i\hat{\phi}_{mn}(z,r);\hat{\eta}_{mn}(s_0)]\,e^{im\theta - i\omega_{mn}t}, \tag{20}$$

where ω_{mn} are the eigenfrequencies, $[\hat{\phi}_{mn}(z,r);\hat{\eta}_{mn}(s_0)]$ denote the eigenvectors, and A_{mn} their amplitudes, which are determined by the initial conditions. Note that m is the number of nodes in the azimuthal directions while n is the number of nodes in the longitudinal direction. We shall particularly consider theoretical modes $(m,n) = (1,0)$, $(0,1)$, $(1,1)$, and $(0,2)$ that are expected to correspond to experimental modes $1s$, $0a$, $1a$, and $0s$, respectively.

Introducing two test functions $\phi^*(r,z)$ and $\eta^*(s_0)$, the problem is written in variational formulation as follows:

$$-\int\!\!\int_\Omega \phi^*\cdot\Delta\hat{\phi} r dr dz + \int_{\mathcal{S}} \phi^*\cdot\left(\mathbf{n}_0\cdot\nabla\hat{\phi}_{mn} - \omega\hat{\eta}_{mn}\right) r ds_0 + \int_{\mathcal{S}} \eta^*\left(\frac{\gamma}{\rho}K_1(\hat{\eta}_{mn}) - \omega\hat{\phi}_{mn}\right) r ds_0 = 0. \tag{21}$$

Integrating by parts the Laplacian and the term involving the second derivative of η in the expression for K_1 and dropping indices (mn) for simplicity yields

$$\begin{aligned}
&\omega\left[\int_{\mathcal{S}}\left(\eta^*\hat{\phi} + \phi^*\hat{\eta}\right) r ds_0\right] \\
&= \int\!\!\int_\Omega \left(\nabla\phi^*\cdot\nabla\hat{\phi} + \frac{m^2}{r^2}\phi^*\hat{\phi}\right) r dr dx + \frac{\gamma}{\rho}\int_{\mathcal{S}}\frac{\partial\eta^*}{\partial s_0}\frac{\partial\hat{\eta}}{\partial s_0} r ds_0 \\
&\quad - \frac{\gamma}{\rho}\int_{\mathcal{S}}\eta^*\left(\left[\frac{\partial\alpha}{\partial s_0}\right]^2 + \frac{\cos^2\alpha}{r^2} - \frac{m^2}{r^2}\right)\eta^*\hat{\eta} r ds_0.
\end{aligned} \tag{22}$$

This eigenvalue problem is discretized using finite elements. A mesh is first generated by a triangulation of the domain Ω based on the mean shape $\mathcal{S}$ computed by the method detailed in Sec. IV A. Volume functions ϕ and ϕ^* are discretized by projection along a basis of two-dimensional P1 elements while surface functions η and η^* are discretized along a basis of one-dimensional P1 elements. This results in a matrix equation of the form $AX = \omega BX$, which is solved by means of a shift-and-invert method. The numerical implementation is realized using the FreeFem++ software, a tool which has proved its efficiency for linearized hydrodynamic problems such as wake instabilities past bluff bodies[26] or path instability of moving bodies.[29] The present implementation for the surface unknown functions η and η^* is close to the one used and described in Refs. 27 and 28 for the study of sloshing modes of a free surface swirling flow.

C. Validations

The validation of the numerical computation has been carried out by considering two particular cases for which an analytical solution is available. The first case is a spherical drop that is anchored at the poles ($(z,r) = (0,0)$ and $(L,0)$), which is equivalent to a free oscillating sphere provided we consider only non-axisymmetric modes ($n \neq 0$). Because their nodes are located at the poles, these modes naturally satisfy the constraint of attachment. The problem of a free liquid sphere was first solved by Rayleigh and generalized by Lamb.[18] The equilibrium shape is a sphere of radius R_0, the eigenvectors are the spherical harmonics Y_{lm} and the eigenfrequencies are given by

$$\omega_l^* = \sqrt{l(l-1)(l+2)}\sqrt{\frac{\gamma}{\rho R_0^3}}. \tag{23}$$

Note that the eigenfrequencies of an oscillating sphere only depend on the principal wavenumber l, which is equal to $m+n$ when using the notation used here to describe a liquid bridge. For the

TABLE I. Eigenfrequencies of a sphere anchored at both poles. Analytical solution ω_l^* given by Eq. (23) compared to numerical results ω_{mn} for various eigenmodes.

l = m + n	ω_l^*/ω_R	ω_{1n}/ω_R	ω_{2n}/ω_R	ω_{3n}/ω_R
2	0.089 44	0.091 08 ($n=1$)	0.089 45 ($n=0$)	
3	0.173 20	0.176 74 ($n=2$)	0.173 26 ($n=1$)	0.173 21 ($n=0$)
4	0.268 33	0.274 77 ($n=3$)	0.268 35 ($n=2$)	0.268 35 ($n=1$)
5	0.374 16	0.384 51 ($n=4$)	0.374 60 ($n=3$)	0.374 22 ($n=2$)

validation using the present numerical method, we replaced the anchoring condition at the poles by the boundary conditions used for bridges, assuming that the sphere is held by two disks of radius R with $R/R_0 = 0.1$. Table I compares the computed eigenfrequencies ω_{mn} to the analytical expression of ω^*_{m+n} given by (23) for several values of m and n. The agreement is very satisfactory, especially for $m \geq 2$. The slight discrepancies for $m = 1$ can be attributed to the replacement of the anchoring condition at the pole by a pinning condition at disks of finite size.

The second validation case corresponds to the oscillations of a cylindrical bridge ($V^* = 1$). For this case, we were able to solve the problem using a different, semi-analytical method which is described in Appendix C. Table II compares the eigenfrequencies computed by both approaches. Again, the agreement is excellent, giving further confidence in the finite-elements method used in the sequel.

D. Results for non-cylindrical bridges

The numerical method can now be used for the non-cylindrical bridges resulting from the coalescence of two drops, with mean shapes as computed and discussed in Sec. IV A. Figure 11 shows the eigenfrequencies of the four modes 0a ($m = 0, n = 1$), 0s ($m = 0, n = 2$), 1a ($m = 1, n = 1$), and 1s ($m = 1, n = 0$) as a function of the slenderness ratio L^*. Both the results corresponding to a cylindrical bridge ($V^* = 1$) and to non-cylindrical one (V^* given by Eq. (1)) are presented.

When looking at the experimental results, we saw in Figure 10 that measured frequencies normalized by ω_R were strongly decreasing functions of L^*. In Figure 11, eigenfrequencies have been normalized by $\omega_L = \sqrt{\gamma/\rho L^3}$ to see whether L could be a more relevant length to define a frequency scale. It is clearly not the case for a cylindrical bridge since ω_{1s}/ω_L and ω_{1a}/ω_L strongly increase with L^* while ω_{0s}/ω_L and ω_{0a}/ω_L strongly decrease. In particular, the value of ω_{0a} crosses

TABLE II. Eigenfrequencies of a finite bridge with a cylindrical equilibrium shape for various oscillation modes and slenderness ratios L^*. Bold characters: semi-analytical results (Appendix A); regular characters: numerical results using finite-element method. Semi-analytical results were computed by truncating the series (B13) and (B14) to 20 terms, and numerical results using a grid with average mesh size $\Delta x = 0.02R$.

	ω_{01}/ω_R mode 0a	ω_{02}/ω_R mode 0s	ω_{03}/ω_R ⋯	ω_{10}/ω_R mode 1s	ω_{11}/ω_R mode 1a	ω_{12}/ω_R ⋯
$L^*=2$	**3.2646**	**7.5231**	**12.7978**	**1.6744**	**4.3053**	**8.2671**
	3.2657	7.5303	12.8207	1.6746	4.3069	8.2749
$L^*=3$	**1.4416**	**3.7080**	**6.5740**	**1.0990**	**2.5516**	**4.5999**
	1.4418	3.7096	6.5794	1.0990	2.5520	4.6018
$L^*=4$	**0.7345**	**2.1318**	**3.9766**	**0.8144**	**1.8046**	**3.1056**
	0.7346	2.1323	3.9784	0.8144	1.8048	3.1063
$L^*=5$	**0.3761**	**1.3214**	**2.6117**	**0.6459**	**1.3941**	**2.3252**
	0.3761	1.3216	2.6187	0.6459	1.3942	2.3256
$L^*=6$	**0.1298**	**0.8449**	**1.8089**	**0.5350**	**1.1353**	**1.8531**
	0.1298	0.8450	1.8092	0.5350	1.1353	1.8533

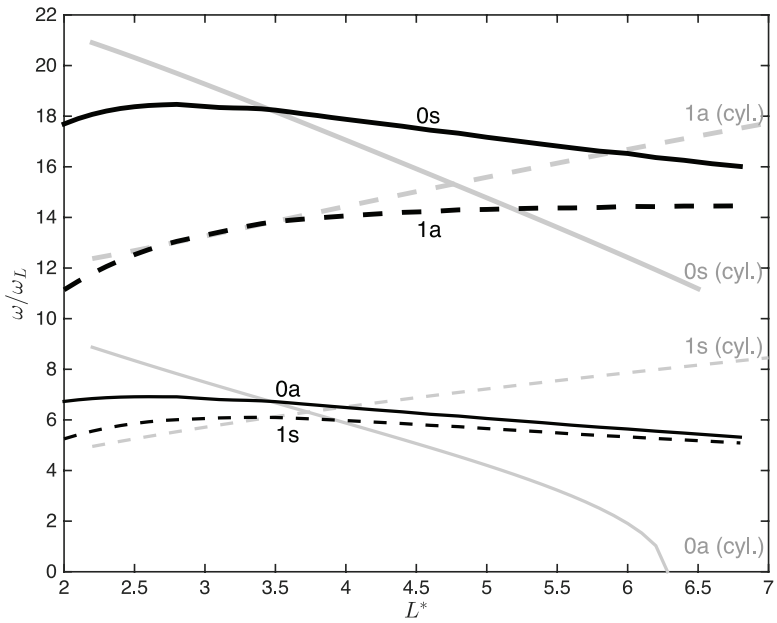

FIG. 11. Normalized theoretical eigenfrequencies, ω_{ij}/ω_L, of a cylindrical bridge (grey lines) and of a bridge resulting of the coalescence of two drops (black lines) for modes 0s, 0a, 1s, and 1a.

zeros at $L^* = 2\pi$, which means that the equilibrium shape becomes unstable and that a bridge of longer length should break. Eigenfrequencies for a bridge resulting from the coalescence of two drops follow a different trend and coincide with those of the cylindrical case only at $L^* = L_c \approx 3.46$, where the bridge is indeed cylindrical. None of the frequencies approaches zero, which indicates that the fact that the bridge becomes more and more convex as L^* increases retards the onset of the instability. As already commented on experimental results, the modes can be grouped into pairs. Modes 1a and 0s have larger frequencies and converge towards each other at large L^*. Modes 1s and 0a have lower frequencies which are close to each other over the whole range of L^* investigated. Moreover, we remark that the evolutions ω_{mn}/ω_L with L^* are rather flat for the four considered modes, suggesting that L is a better length scale than R to build a characteristic frequency. The discussion about the best characteristic length scale will be continued in Sec. V.

V. DISCUSSION

Given that the experimental results are found independent of the radius R of the capillaries, of the presence of $MgSO_4$ and of differences in the initial size of the two bubbles, the different cases are no longer distinguished and we will consider that the amplitude of the oscillations has no influence on the measured eigenfrequencies and damping rates. Comparisons with theoretical prediction assuming small amplitudes are therefore relevant.

Experimental and theoretical frequencies of the four considered modes are shown in Figure 12 as a function of the slenderness ratio L^*. Overall, owing to the assumptions made in the theory and the difficulty to precisely align the capillaries in experiment, the agreement is very satisfactory. Some disparities between experiments and theory are visible for short bridges of concave shape ($L < 3.46$) especially for mode 0s. We suspect viscous effects localized close to the ending disks to be the cause of these differences. For long bridge with convex shapes ($L^* > 3.46$), the agreement is good for all modes. It is therefore reasonable to conclude that the present experimental method allows the investigation of the eigenmodes of oscillations predicted by the linear inviscid theory.

Comparisons between theoretical modes of cylindrical and non-cylindrical bridges have revealed a strong influence of the mean shape (Figure 11). To consider a length scale characteristic

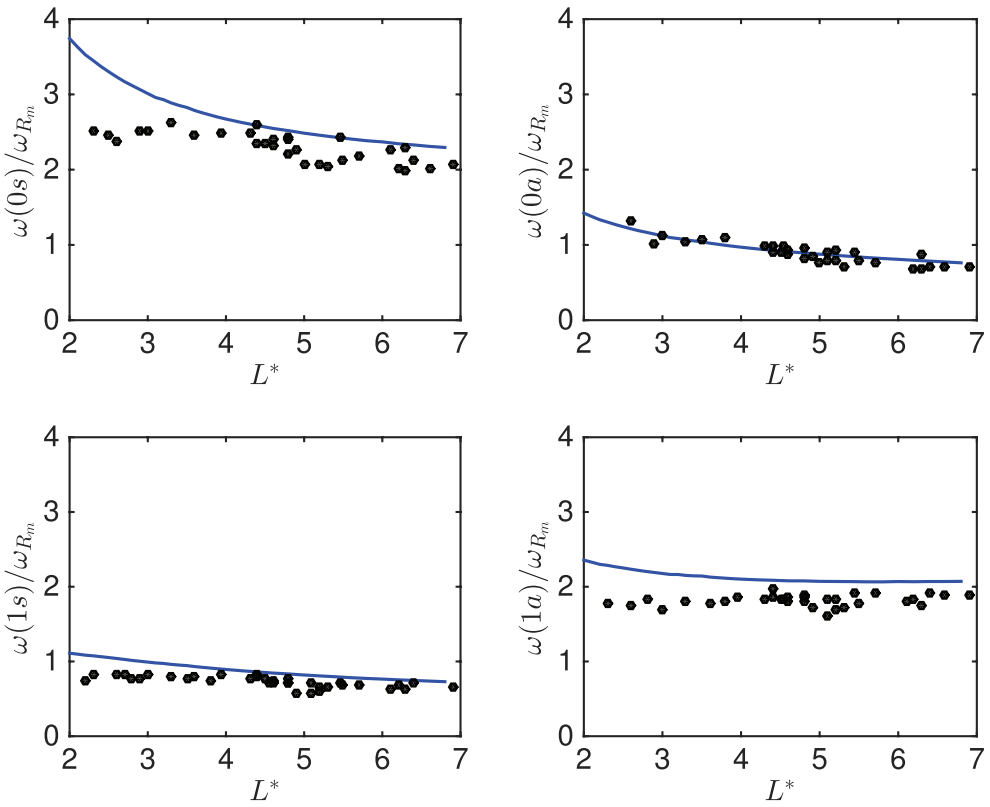

FIG. 12. Eigenfrequencies of modes 0s, 0a, 1s, and 1a normalized by $\omega_{R_m} = \sqrt{\gamma/\rho {R_m}^3}$. Symbols: experiments. Lines: theoretical predictions.

of the shrunk/swollen character of the mean shape may thus help the interpretation of the results. The radius R_m at the middle of the bridge seems a good candidate since it is almost proportional to L, which was itself found to be rather good scale to characterize the eigenfrequencies of non-cylindrical bridges. In Figure 12, all frequencies have been normalized by $\omega_{Rm} = \sqrt{\gamma/\rho R_m^3}$. It is remarkable to observe that, with such a normalization, the measured frequencies of the four modes become almost independent of L. Practically, this means that the frequencies ω_{ij}/ω_{R_m} are found to be almost the same whatever are the values of R or L. The mass of fluid involved in the oscillations of a bridge resulting from the coalescence of two droplets is therefore proportional to ρR_m^3.

In the range of Ohnesorge number investigated, the problem is almost inviscid. The role of viscosity is limited to cause a weak dissipation that slowly damps the oscillations. As for the case of the oscillations of a drop in a vacuum,[18] the dissipation of the mechanical energy can be calculated from the potential flow field. Assuming that the potential flow is characterized by the length scale R_m, the damping rate of all modes should scale as $\beta_{R_m} = \mu/\rho R_m^2$. Figure 13 shows the measured damping normalized by β_{R_m}. Compared to Figure 10(b), the evolutions of β_{ij}/β_{R_m} s are rather flat, indicating that the dependence of the damping rate with L^* is mostly accounted for by β_{R_m}. However, the scatter is too large to allow a definitive conclusion. Moreover, it is probable that dissipation in the vicinity of the ending disks plays a role that cannot be accounted for by the viscous potential flow approximation. This point should be decided by including viscous effect in the theory.

To conclude, we want to stress that the present method, which combines theory and experiments, has been proved to be well suited to reveal the fundamental dynamic characteristics of bridge oscillations. It can be used in future work to investigate complex systems to get insights into liquid fracture and high-speed dynamic interfacial rheology.

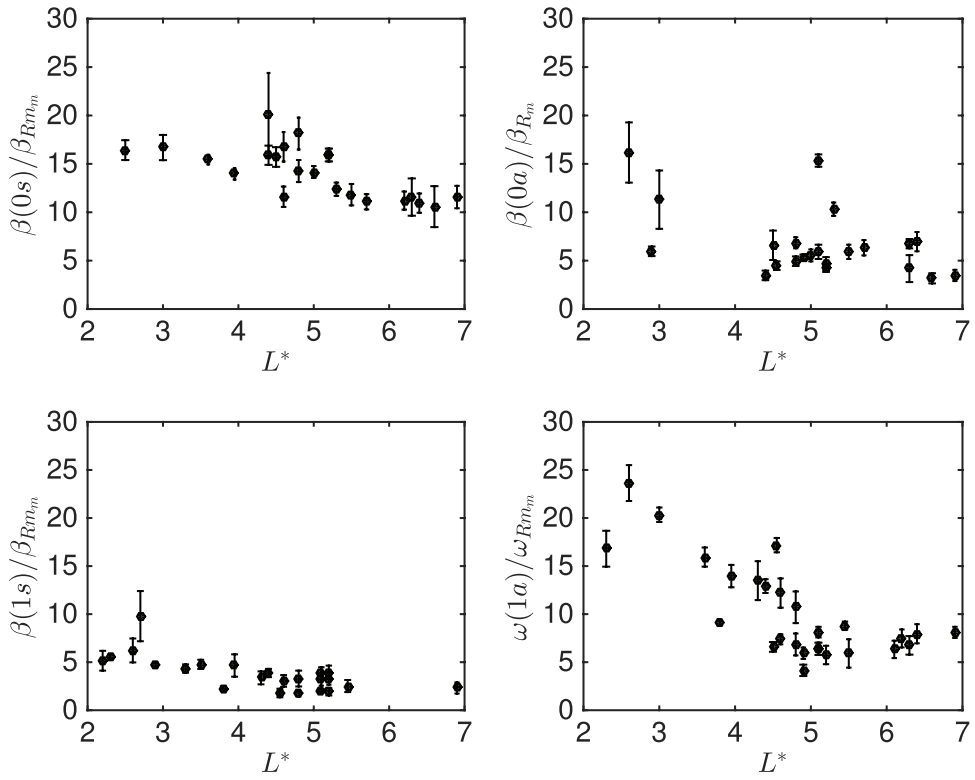

FIG. 13. Experimental damping rate of modes 0s, 0a, 1s, and 1a normalized by $\beta_{R_m} = \mu/\rho R_m^2$.

APPENDIX A: RELATION BETWEEN THE REDUCED VOLUME AND SLENDERNESS RATIO

Prior to coalescence, the two drops are truncated spheres of radius R_g in contact at $z = L/2$ and limited by two disks of radius R (Figure 14). The following relation is found between R_g, R, and L:

$$R_g = \frac{R^2}{L} + \frac{L}{4}, \tag{A1}$$

and the total volume of the two drops is given by

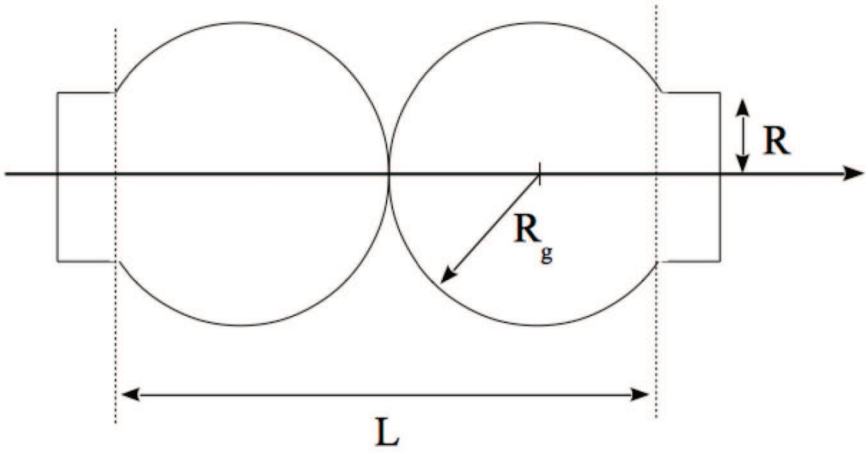

FIG. 14. Schematic of the two drops prior to coalescence.

$$V = \frac{2}{3}\pi\left(\frac{L}{2}\right)^2\left(3R_g - \frac{L}{2}\right). \tag{A2}$$

Substituting the expression of R_g from (A1) into (A2) leads to

$$V = \frac{2}{3}\pi\left(\frac{L}{2}\right)^2\left(3\frac{R^2}{L} + \frac{L}{4}\right). \tag{A3}$$

Considering that the volume of the bridge is the total volume of the two truncated spheres, we obtain the following relation between L^* and V^* which is imposed by the present configuration:

$$V^* = \frac{V}{\pi R^2 L} = \frac{1}{2}\left(1 + \frac{L^{*2}}{12}\right). \tag{A4}$$

APPENDIX B: EXPRESSIONS FOR THE CURVATURE

1. Cylindrical coordinates

We first assume that the free surface admits a parametrization in cylindrical coordinates. We note $r(z)$ the position of the mean surface, and $\eta_r(z,\theta,t)$ the displacement with respect to the mean surface in the *radial direction*. The instantaneous position of the interface is thus given by $G(r,z,\theta,t) = 0$, where G is a distance function defined by $G(r,z,\theta,t) = r - [r(z) + \epsilon\eta_r(z,\theta,t)]$. The normal vector is then deduced as $\mathbf{n} = \frac{\nabla G}{|\nabla G|}$. We assume $\epsilon \ll 1$ and make an expansion in power series of ϵ. Noting z-derivative with primes, e.g., $r' = dr/dz$, and replacing θ-derivatives by im for sake of modal dependence, we get

$$\mathbf{n} = \mathbf{n}_0 + \epsilon\mathbf{n}_1,$$

with

$$\mathbf{n}_0 = \frac{1}{(1+r'^2)^{1/2}}\begin{bmatrix} -r' \\ 1 \\ 0 \end{bmatrix}_{(z,r,\theta)}, \quad \mathbf{n}_1 = \frac{1}{(1+r'^2)^{3/2}}\begin{bmatrix} -\eta_r' \\ -r'\eta_r' \\ im(1+r'^2)/r \end{bmatrix}_{(z,r,\theta)}.$$

The curvature is then given by $K = \nabla \cdot \mathbf{n}$. Expressing this quantity at $r = r(z) + \epsilon\eta_r$ and developing in series with ϵ, we get

$$K = K_0(z) + \epsilon K_1(z),$$

with

$$K_0(z) = -\frac{r''}{(1+r'^2)^{3/2}} + \frac{r'}{r(1+r'^2)^{1/2}} \tag{B1}$$

and

$$K_1(z) = -\frac{1}{(1+r'^2)^{3/2}}\eta_r'' + \left(\frac{3r'r''}{(1+r'^2)^{5/2}} - \frac{r'}{r(1+r'^2)^{3/2}}\right)\eta_r' + \frac{(m^2-1)}{r^2(1+r'^2)^{1/2}}\eta_r. \tag{B2}$$

2. Curvilinear coordinates

We now express the previous expressions for K_0 and K_1 in terms of the curvilinear abscissa s_0 of the mean surface. We note η the displacement in the direction of the normal $\mathbf{n}_0$ to the mean surface. Derivatives with respect to s_0 are denoted by dots, in order to distinguish from z-derivative that are denoted by primes.

Noting $\alpha(s_0)$ the angle between the mean free surface and the x-axis, the following geometrical relations are found in Ref. 30:

$$\dot{z} = \cos\alpha; \quad \dot{r} = \sin\alpha; \quad r' = \frac{\mathrm{d}r}{\mathrm{d}z} = \tan\alpha;$$
$$r'' = \frac{\mathrm{d}\tan\alpha}{\mathrm{d}z} = \frac{\mathrm{d}\tan\alpha}{\mathrm{d}\alpha}\frac{\mathrm{d}\alpha}{\mathrm{d}s_0}\frac{\mathrm{d}s_0}{\mathrm{d}z} = \frac{\dot{\alpha}}{\cos^3\alpha}.$$

Substituting these expressions into (B1), we obtain the following classical formula for the curvature of the mean surface:

$$K_0(s_0) = -\dot{\alpha} + \frac{\cos\alpha}{r}. \tag{B3}$$

We now express the curvature perturbation K_1 in curvilinear coordinates. For that purpose, we first need to express the radial displacement η_r and its z-derivatives in terms of the normal displacement η and its s_0-derivatives. Geometrical considerations and elementary manipulations lead to

$$\eta_r = \frac{\eta}{\cos\alpha};$$
$$\eta_r' = \frac{1}{\cos\alpha}\frac{\mathrm{d}\eta_r}{\mathrm{d}s_0} = \frac{1}{\cos\alpha^2}\dot{\eta} + \frac{\dot{\alpha}\sin\alpha}{\cos\alpha^2}\eta;$$
$$\eta_r'' = \frac{1}{\cos\alpha}\frac{\mathrm{d}\eta_r'}{\mathrm{d}s_0} = \frac{1}{\cos\alpha^3}\ddot{\eta} + \frac{\dot{\alpha}\sin\alpha}{\cos\alpha^2}\eta + \frac{3\dot{\alpha}\sin\alpha}{\cos\alpha^4}\dot{\eta} + \left(\frac{\dot{\alpha}^2(3-2\cos^2\alpha)}{\cos^5\alpha} + \frac{\ddot{\alpha}\sin\alpha}{\cos\alpha^4}\right)\eta.$$

Recasting these expressions into (B2) and rearranging the terms eventually lead to

$$K_1(z) = K_1(s_0) + \frac{\mathrm{d}K_0}{\mathrm{d}s_0}\tan\alpha\,\eta, \tag{B4}$$

where $K_1(s_0)$ is the desired expression of the curvature perturbation in curvilinear coordinates,

$$K_1(s_0) = -\ddot{\eta} - \frac{\sin\alpha}{r}\dot{\eta} + \left(\frac{m^2}{r^2} - \frac{\cos^2\alpha}{r^2} - \dot{\alpha}^2\right)\eta. \tag{B5}$$

The term involving the derivative of K_0 in (B4) accounts for the fact that the direction in which the displacement is measured is different in both parametrizations (see Figure 2).

APPENDIX C: STABILITY AND OSCILLATION FREQUENCIES OF CYLINDRICAL LIQUID BRIDGES

1. Problem formulation

We consider a cylindrical liquid bridge of radius R and length L. R and $\sqrt{\rho R^3/\gamma}$ are used as characteristic length and time for nondimensionalization. The slenderness is defined by $L^* = L/R$. The unknowns are a potential ϕ defined in the volume, and the normal displacement η defined on the surface (extending from $z = 0$ to $z = L^*$). The system to be solved is

$$\mathbf{u} = \epsilon\nabla\phi(z,r)e^{i(m\theta+\omega t)},$$
$$r = R + \epsilon\eta(z)e^{i(m\theta+\omega t)},$$

$$\Delta\phi = 0, \tag{C1}$$
$$\partial_z\phi = 0 \quad \text{for } z = 0 \text{ and } z = L^*, \tag{C2}$$
$$\partial_r\phi = i\omega\eta \quad \text{for } r = 1, \tag{C3}$$
$$\gamma K_1 = \gamma(-\partial_z^2 + m^2 - 1)\eta = i\omega\phi \quad \text{for } r = 1, \tag{C4}$$
$$\eta = 0 \quad \text{for } z = 0 \text{ and } z = L^*. \tag{C5}$$

2. Analytical solution

The method is in the line with that developed by Henderson and Miles[31] for studying sloshing modes in a cylindrical container with a fixed contact line. We first expand the potential as follows

(which automatically satisfies the boundary conditions at $z = 0, L$) :

$$\phi = \sum_{n=0}^{\infty} \phi_n \cos(k_n z) \frac{I_m(k_n r)}{I_m(k_n)} \tag{C6}$$

$$= \sum_{n=0}^{\infty} \phi_{2n} (-1)^n \cos(k_{2n} z') \frac{I_m(k_{2n} r)}{I_m(k_{2n})} + \sum_{n=0}^{\infty} \phi_{2n+1} (-1)^n \sin(k_{2n+1} z') \frac{I_m(k_{2n+1} r)}{I_m(k_{2n+1})}, \tag{C7}$$

where $k_n = n\pi/L^*$.

The second expression is expressed in terms of $z' = z - L/2$, which spans the bridge from $-L/2$ to $L/2$. In terms of this centered variable, this expression allows to separate the symmetrical and anti-symmetrical components, which contain, respectively, only even and odd terms. However, in what follows, we stay with the first expression in terms of z, in order to avoid mixing between sines and cosines. We first work with the dynamic boundary condition which can be written in the following form:

$$\gamma(-\partial_z^2 + m^2 - 1)\eta = \sum_{n=0}^{\infty} (i\omega)\phi_n \cos(k_n z). \tag{C8}$$

Unless if the right-hand side contains resonant terms (see below), the solution of this equation will be generally written as follows:

$$\eta = \sum_{n=0}^{\infty} A_n \cos(k_n z) - (A_s C_s(z) + A_a C_a(z)) . \tag{C9}$$

We recognize two parts. The first is the solution proportional to the forcing terms, with amplitudes A_n,

$$A_n = \frac{-i\omega\phi_n}{\gamma(k_n^2 + m^2 - 1)}.$$

The second part is the solution of the homogeneous equation. This part contains two auxiliary functions, noted $C_s(z)$ and $C_a(z)$. These functions are chosen so that $C_s(z)$ is symmetric and $C_a(z)$ is antisymmetric, and are normalized such that $C_s(0) = C_a(0) = 1$. Physically, these two functions represent displacements of the free surface which do not modify the mean curvature. The expressions for these functions depend upon m and will be given below.

We now consider the kinematic boundary condition, which yields

$$\eta = (i\omega)^{-1} \sum_{n=0}^{\infty} \phi_n \cos(k_n z) T_n, \quad \text{with } T_n = \frac{I_m'(k_n)}{I_m(k_n)}. \tag{C10}$$

Using the previous expression for A_n, this expression leads to

$$\eta = \sum_{n=0}^{\infty} \left(\frac{\omega_n^*}{\omega}\right)^2 A_n \cos(k_n z), \tag{C11}$$

where

$$(\omega_n^*)^2 = \left(k_n^2 + m^2 - 1\right) T_n$$

are the *free* frequencies, i.e., the eigenfrequencies that would be obtained if we remove the boundary condition of anchoring of the contact line. We now have two different expressions for $\eta(z)$, namely, (C9) and (C11), and must equate them. One clearly sees that if the complementary functions are absent, the solution is trivially $\omega = \omega_n^*$, which means that the Fourier components are uncoupled and the frequencies are those of *free problem*. These modes do not verify the condition of fixed line, but instead they verify $\partial_z \eta = 0$; physically, this represents a bridge located between two parallel planes and allowed to slip along them. When the constraint of fixed line is imposed, the complementary

functions have to be introduced. To equate the two expressions for η, these functions have to be decomposed along the Fourier basis. The decomposition is as follows:

$$C_s(z) = \sum_{n=0}^{\infty} C_n^s \cos(k_{2n} z),$$
$$C_a(z) = \sum_{n=0}^{\infty} C_n^a \cos(k_{2n+1} z).$$

The Fourier coefficients will be given below. We can now treat separately the symmetric and antisymmetric parts of the expression for η. For symmetric perturbations, equating the Fourier coefficients leads to

$$\left(\frac{\omega_{2n}^*}{\omega}\right)^2 A_{2n} = A_{2n} + A_s C_n^s, \tag{C12}$$

which can also be written as

$$A_{2n} = A_c C_n^s \left(\frac{\omega^2}{\omega^2 - \omega_{2n}^*}\right).$$

It remains to sum over all indices n, and recognize that $\sum A_{2n} = A_s$ (which comes from the fixed-line condition $\eta(0) = 0$), to get the following dispersion relation:

$$F_s(\omega^2) = \sum C_n^s \left(\frac{\omega^2}{\omega^2 - \omega_{2n}^*}\right) = 1. \tag{C13}$$

The case of antisymmetric modes is similar and yields

$$F_a(\omega^2) = \sum C_n^a \left(\frac{\omega^2}{\omega^2 - \omega_{2n+1}^*}\right) = 1. \tag{C14}$$

We can note that the functions F_s and F_a change sign through an infinite branch at the *free* frequencies ω_n^* and are monotonous between these roots; so we can conclude that the frequencies for the fixed-line problem lie between those for the free-line problem.

3. Details about Fourier coefficients

- For $m = 0$, the auxiliary functions are given as

$$C_s(z) = \frac{\cos(z - L^*/2)}{\cos(L^*/2)}; \quad C_a(z) = \frac{\sin(L^*/2 - z)}{\sin(L^*/2)}. \tag{C15}$$

  The Fourier coefficients for these functions are as follows:

$$C_n^s = \frac{4L^*}{L^{*2} - \pi^2(2n)^2} \tan(L^*/2) \quad \text{if } n \neq 0,$$
$$C_0^s = \frac{2}{L^*} \tan(L/2),$$
$$C_n^a = -\frac{4L^*}{L^{*2} - \pi^2(2n+1)^2} \cot(L^*/2).$$

  Note that if $L^* = n\pi$, the problem for η becomes non-homogeneous and a special treatment is required. However, these cases are of no particular significance, so we omit the details.
- For $m \geq 2$, the auxiliary functions are given as by

$$C_s(z) = \frac{\cosh(\mu(z - L^*/2))}{\cosh(\mu L^*/2)}; \quad C_a(z) = \frac{\sinh(\mu(L^*/2 - z))}{\sinh(\mu L^*/2)}, \tag{C16}$$

with $\mu = \sqrt{m^2 - 1}$. The Fourier coefficients for these functions are as follows:

$$C_n^s = \frac{4L^*\mu}{\mu^2 L^{*2} + \pi^2(2n)^2} \tanh(\mu L^*/2) \quad \text{if } n \neq 0,$$

$$C_0^s = \frac{2}{L^*} \tanh(L^*/2),$$

$$C_n^a = \frac{4L^*\mu}{\mu^2 L^{*2} + \pi^2(2n+1)^2} \coth(\mu L^*/2).$$

- The case $m = 1$ requires a specific treatment. In that case, the left-hand side of Eq. (C8) is simply $\partial_x^2 \eta = 0$, the homogeneous solutions of which are constant or linear functions, but the right-hand side contains the constant term $i\omega\phi_0$ which is proportional to the homogeneous solution, hence, resonant. In that case, the auxiliary function $C^s(x)$ has to be taken as the response to this resonant term, namely,

$$C_s(z) = (2z/L^* - 1)^2.$$

The antisymmetric auxiliary function is $C_a(x)$ and is not resonant and is taken as

$$C_a(z) = (1 - 2z/L^*).$$

The Fourier coefficients for these auxiliary functions are

$$C_n^s = \frac{16}{\pi^2 n^2} \quad \text{if } n \neq 0,$$

$$C_0^s = 1/3,$$

$$C_n^a = \frac{8}{\pi^2 n^2}.$$

The solution to the antisymmetric problem is still given by (C14). The symmetric problem is slightly different. In this case, the expressions for A_n given above (C12) are still valid for $n \neq 0$, but the case $n = 0$ is different, and the expressions has to be replaced by

$$A_0 = \left(\frac{8}{\pi^2 L^{*2}} + C_0^s \right) A_s \,.$$

Hence, in this case, the dispersion relation reads

$$F_s(\omega^2) = \left(\frac{8}{\pi^2 L^{*2}} + \frac{1}{3} \right) + \sum_{n=1}^{\infty} C_n^s \left(\frac{\omega^2}{\omega^2 - \omega_{2n}^{*}} \right) = 1. \tag{C17}$$

[1] J. Eggers, "Nonlinear dynamics and breakup of free-surface flows," Rev. Mod. Phys. **69**, 865-929 (1997).
[2] Lord Rayleigh, "On the instability of jets," Proc. London Math. Soc. **10**, 4-13 (1878).
[3] Lord Rayleigh, "On the capillary phenomena of jets," Proc. R. Soc. London **29**, 71-97 (1879).
[4] E. Villermaux, "Fragmentation," Annu. Rev. Fluid Mech. **39**(1), 419 (2006).
[5] F. Risso and J. Fabre, "Oscillations and breakup of a bubble immersed in a turbulent field," J. Fluid Mech. **372**, 323-355 (1998).
[6] S. Galinat, F. Risso, O. Masbernat, and P. Guiraud, "Dynamics of drop breakup in inhomogeneous turbulence at various volume fractions," J. Fluid Mech. **578**, 85–94 (2007).
[7] C. A. Miller and L. E. Scriven, "The oscillations of a fluid droplet immersed in another fluid," J. Fluid Mech. **32**, 417 (1968).
[8] A. Prosperetti, "Free oscillations of drops and bubbles: The initial-value problem," J. Fluid Mech. **100**, 333 (1980).
[9] M. Strani and F. Sabetta, "Free vibrations of a drop in partial contact with a solid support," J. Fluid Mech. **141**, 233-247 (1984).
[10] M. Strani and F. Sabetta, "Viscous oscillations of a supported drop in an immiscible fluid," J. Fluid Mech. **189**, 397-421 (1988).
[11] J. B. Bostwick and P. H. Steen, "Capillary oscillations of a constrained liquid drop," Phys. Fluids **21**, 32108 (2009).
[12] A. Prosperetti, "Linear oscillations of constrained drops, bubbles, and plane liquid surfaces," Phys. Fluids **24**, 032109 (2012).
[13] J. Vejrazka, L. Vobecka, and J. Tihon, "Linear oscillations of a supported bubble or drop," Phys. Fluids **25**, 062102 (2013).
[14] B. Lalanne, S. Tanguy, and F. Risso, "Effect of rising motion on the damped shape oscillations of drops and bubbles," Phys. Fluids **5**, 112107 (2013).
[15] E. Trinh, A. Zwern, and T. G. Wang, "An experimental study of small-amplitude drop oscillations in immiscible liquid systems," J. Fluid Mech. **115**, 453 (1981).
[16] N. A. Chebel, F. Risso, and O. Masbernat, "Inertial modes of a periodically forced buoyant drop attached to a capillary," Phys. Fluids **23**, 102104 (2011).

[17] N. A. Chebel, J. Vejrazka, O. Masbernat, and F. Risso, "Free oscillations of an oil drop rising in water: Effect of surface contamination," J. Fluid Mech. **702**, 533-542 (2012).
[18] H. Lamb, *Hydrodynamics*, 6th ed. (Cambridge University Press, Cambridge, England, 1932).
[19] A. Nicolás and J. M. Vega, "Linear oscillations of axisymmetric viscous liquid bridges," Z. Angew. Math. Phys. **51**, 701 (2000).
[20] E. J. Vega and J. M. Montanero, "Damping of linear oscillations in axisymmetric liquid bridges," Phys. Fluids **21**, 092101 (2009).
[21] L. A. Slobozhanin and J. M. Perales, "Stability of liquid bridges between equal disks in an axial gravity field," Phys. Fluids A **5**, 1305 (1993).
[22] J. Meseguer, L. A. Slobozhanin, and J. M. Perales, "A review on the stability of liquid bridges," Adv. Space Res. **16**, 5 (1995).
[23] P. Guillot, A. Colin, A. S. Utada, and A. Ajdari, "Stability of a jet in confined pressure-driven biphasic flows at low Reynolds numbers," Phys. Rev. Lett. **99**(10), 104502-104505 (2007).
[24] I. Martinez, "Floating zone equilibrium shapes and stability criteria," in *COSPAR: Space Research*, edited by M. J. Rycroft and A. C. Stickland (Pergamon, 1978), Vol. XVIII, pp. 519-522.
[25] K.-H. Tsao and D. L. Koch, "Collisions of slightly deformable, high Reynolds number bubbles with short-range repulsive forces," Phys. Fluids **6**, 2591-2625 (1994).
[26] D. Sipp and A. Lebedev, "Global stability of base and mean-flows: A general approach and its applications to cylinder and open cavity flows," J. Fluid Mech. **593**, 333-358 (2007).
[27] J. Mougel, D. Fabre, and L. Lacaze, "Waves and instabilities in rotating free surface flows," Mech. Ind. **15**, 107-112 (2014).
[28] L. Tophøj, J. Mougel, T. Bohr, and D. Fabre, "The rotating polygon instability of a swirling free-surface flow," Phys. Rev. Lett. **110**, 194502 (2013).
[29] J. Tchoufag, D. Fabre, and J. Magnaudet, "Global linear stability analysis of the wake and path of buoyancy-driven discs and thin cylinders," J. Fluid Mech. **740**, 278-311 (2014).
[30] P. G. de Gennes, F. Brochard-Wyart, and D. Quéré, *Capillarity and Wetting Phenomena* (Springer, 2004).
[31] D. M. Henderson and J. W. Miles, "Surface-wave damping in a circular cylinder with a fixed contact line," J. Fluid Mech. **275**, 285-299 (1994).